



The interplay between corrosion and cracks in reinforced concrete beams with non-uniform reinforcement corrosion

Downloaded from: <https://research.chalmers.se>, 2026-04-03 10:21 UTC

Citation for the original published paper (version of record):

Gil Berrocal, C., Fernandez, I., Rempling, R. (2022). The interplay between corrosion and cracks in reinforced concrete beams with non-uniform reinforcement corrosion. *Materials and Structures/Materiaux et Constructions*, 55(4).
<http://dx.doi.org/10.1617/s11527-022-01956-2>

N.B. When citing this work, cite the original published paper.



The interplay between corrosion and cracks in reinforced concrete beams with non-uniform reinforcement corrosion

Carlos G. Berrocal · Ignasi Fernandez · Rasmus Rempling

Received: 19 November 2021 / Accepted: 3 April 2022
© The Author(s) 2022

Abstract This paper investigates the interplay between corrosion of reinforcement and corrosion-induced cracking in reinforced concrete structures with non-uniform corrosion distribution based on the experimental results of a concrete beam simultaneously subjected to sustained deflection and accelerated corrosion through impressed current. Unlike previous studies, this work encompasses various refined techniques for the measurement of surface cracks, such as digital image correlation and distributed optical fiber sensors, as well as for the assessment of reinforcement corrosion, namely 3D laser scanning, to explore previously hidden aspects of the relationship between the two parameters. The applied techniques proved very effective in providing an unprecedented level of detail of both the crack development and corrosion distribution. More specifically, the formation and propagation of corrosion-induced cracks were accurately and constantly monitored over time and subsequently compared to the distribution of corrosion. The

results revealed that determining the maximum corrosion level or even the location of the section with maximum corrosion based solely on visual inspection of the surface crack width may not be possible. However, the width of corrosion-induced cracks was found to increase linearly with the local corrosion level, implying that crack width monitoring can still be used to estimate the rate of corrosion degradation.

Keywords Reinforced concrete · Corrosion · Cracking · Crack width

1 Introduction

Reinforced concrete (RC) is currently the most widely used construction material in the world due to its low cost and the availability of its source components. However, as society pushes for a more responsible construction sector, other aspects are rapidly gaining more relevance in the design and choice of structural materials. For civil infrastructure, three aspects that are central for the development of a sustainable built environment are resource efficiency, accessibility, and durability, all of which are directly affected by ageing and degradation. As a result, the development of monitoring systems and assessment methods that enable a detailed description of a structure's condition are becoming increasingly important.

C. G. Berrocal (✉) · I. Fernandez · R. Rempling
Division of Structural Engineering, Chalmers University
of Technology, 41296 Göteborg, Sweden
e-mail: carlos.gil@chalmers.se

C. G. Berrocal
Thomas Concrete Group AB, Södra Vägen 28,
41254 Göteborg, Sweden

R. Rempling
NCC Sverige AB, Stockholm, Sweden



Among the different deterioration mechanisms impairing the durability of RC structures, corrosion of reinforcement is the most widespread problem worldwide. Corrosion of steel in concrete is usually initiated by the loss of alkalinity in the concrete cover due to carbonation or by a local break-down of the passive layer due to the ingress of chloride ions [1]. The cover thickness and the quality of the concrete are the main parameters controlling the initiation of corrosion in uncracked concrete elements [2]; yet in practice, mechanical loading, temperature gradients, restraint forces or a combination thereof, often results in the formation of cracks, which are known to favour the ingress of deleterious agents and thus promote a premature onset of the corrosion process [3]. Once corrosion has initiated, active dissolution of steel occurs at the reinforcement, which causes a reduction of its cross-sectional area and negatively affects the load-bearing capacity and ductility of the structure, thereby compromising its safety [4].

Determining the actual cross-section of reinforcement in a corroded structure is central to provide an accurate estimation of its residual load-carrying capacity. Although several electro-chemical non-destructive testing techniques exist to estimate the corrosion rate of corroding reinforcement in concrete [5], e.g. linear polarization resistance, galvanostatic pulse or electrochemical impedance spectroscopy, these are only able to provide a snapshot of the corrosion rate at the moment of the measurement. On the other hand, the accumulation of corrosion products at the steel–concrete interface leads to the formation of longitudinal corrosion-induced cracks, which in advanced stages of corrosion can result in spalling of the concrete cover. Such cracks are the clearest sign of active reinforcement corrosion while their width is closely related to the actual corrosion level. Consequently, establishing a well-defined relationship between the corrosion level and the width of corrosion-induced cracks would greatly facilitate the assessment of a structure's condition based on visual inspection.

The relationship between the corrosion level at the reinforcement and the width of corrosion-induced cracks has been investigated in numerous studies over the past three decades, see e.g. [6–16]. Nevertheless, a large scatter exists among the results obtained from different studies, as recently discussed in [17, 18]. Such scatter can be partly ascribed to the varying test

setups, specimen geometries and experimental procedures used by different authors, such as variable cover depth to diameter ratios, different impressed anodic currents, or different loading conditions. In some cases, results from naturally corroded specimens over much longer periods [8, 16] or even from decommissioned structures [18] have also been reported, which may be another source of discrepancy. However, the lack of refined techniques for measuring crack widths and assessing the reinforcement corrosion in a detailed and consistent manner might have also contributed to the observed scatter.

Indeed, most of the available studies in the literature report having used quite rudimentary techniques to determine the surface crack widths, ranging from crack comparator cards [14, 19] and graduated magnifying lenses [6, 8, 16] to mechanical gauges [10–12], with a few exceptions where potentiometers or displacement transducers were installed to track already formed cracks, see e.g. [7]. All of these techniques have in common that they only enable the measurement of cracks at discrete points and, with the exception of the latter type of measurements, they are unable to provide a continuous description of the crack growth over time.

Similarly, the evaluation of the corrosion level has been mostly treated in a very rough manner assuming a uniform distribution of corrosion calculated using Faraday's law based on the applied anodic current [9, 12] or based on gravimetric mass loss measurements [6, 7, 10, 11, 13, 14]. It is worth noting the work by Prof. François and his team, where they determined the mass loss of small segments by gravimetric methods in an effort to provide a description of the corrosion distribution [8, 16]. On the other hand, in the recent years, the use of laser scanners has emerged as a powerful tool enabling a description of the reinforcement corrosion distribution with unprecedented resolution, see e.g. [18, 20–22].

The main aim of this paper is to investigate, experimentally, the relationship between corrosion-induced cracking and the distribution of corrosion at the reinforcement using novel measurement techniques that enable a reliable and precise evaluation of such parameters. In particular, this work combines the use of 3D laser scanning for the detailed description of the reinforcement corrosion with refined techniques for the measurement of cracks, such as digital image correlation (DIC) and distributed optical fiber sensors



(DOFS), that can accurately track the formation and growth of longitudinal corrosion-induced cracks in reinforced concrete elements with non-uniform corrosion distribution. To the authors knowledge, the combination of such techniques has not yet been used for that purpose. In the following sections, a description of the experimental programme, a discussion of the test results and the main findings of the study are provided.

2 Experimental programme

The tests presented in this paper are part of a larger experimental programme comprising 6 large-scale reinforced concrete beams and devised to investigate the capabilities of novel measurement techniques in the performance assessment of reinforced concrete elements subjected to long-term loading and deterioration. This paper focuses on elucidating the interplay between corrosion of reinforcement and corrosion-induced cracking based on the results of one reinforced concrete beam subjected to simultaneous sustained deflection and accelerated corrosion over a period of 67 days. The most important aspects of the experiments are described below.

2.1 Geometry and reinforcement layout

The beam specimen used in this work featured a total length of 3 m and a rectangular cross-section of 200×250 mm. The longitudinal reinforcement consisted of three $\varnothing 16$ mm rebar at the bottom and two $\varnothing 10$ mm at the top. Six $\varnothing 8$ mm closed-loop stirrups were placed on either side of the beam at a spacing of 200 mm. All reinforcement was made of normal ductility carbon-steel (B500B) with a nominal yield strength of 500 MPa. Plastic spacers were placed between the stirrups and the bottom and lateral sides of the form to ensure a clear concrete cover of 20 mm. The ends of the bottom bars were bent upwards to improve the anchorage. Moreover, the bars protruded from the concrete surface at one of the ends in order to enable an electrical connection for the impressed current procedure. The geometry and reinforcement layout of the beams is presented in Fig. 1.

The concrete mix used had a water-to-cement ratio (w/c) of 0.45 and included a sulphate resistant Portland cement with low C_3A content and moderate heat

development. After casting, the beam was covered with a polyethylene sheet to reduce moisture evaporation and stored in an indoor climate (20 ± 2 °C and $60 \pm 10\%$ RH) for 15 days until it was pre-cracked. Thereafter, the beam remained in the same indoor climate for 6 months before the long-term loading began. The concrete compressive strength at 28 days was 68.2 MPa ($CoV = 5.6\%$) based on tests performed in accordance with EN 12390-3:2009 [23] on three 150 mm cubes.

2.2 Test setup and instrumentation

The beam was loaded using a four-point bending setup. Prior to the long-term loading procedure, the beam was subjected to two load cycles up to a total load of 60 kN (corresponding to about 30% of the estimated ultimate capacity), to induce cracking. During the pre-cracking procedure, the crack pattern and maximum crack width of each individual crack formed in the constant moment region were accurately documented using a Digital Image Correlation (DIC) system. Those results were also used to validate a novel approach to quantify deflections and crack widths based on distributed optical fiber sensors as reported in [24].

For the long-term loading, the beam was clamped together with an identical beam as illustrated in Fig. 2a. In that setup, the bottom beam was turned upside down so that the tensile reinforcement was facing upwards. Then the top beam was positioned onto two sets of support plates resting on the bottom beam, the centres of which were 2700 mm apart. Thereafter, the load was introduced at two loading points where the clamping devices were mounted, dividing the total span into three equal spans of 900 mm. Sustained deflection was applied by imposing a constant deformation between the two beams, which was achieved by tightening a threaded bolt screwed into the clamping device. Two load cells were provisioned at the loading points over the top beam and one additional load cells was placed between the support plates at one of the ends in order to ensure a symmetric distribution of load.

After 96 days of imposed deflection, accelerated corrosion of the bottom beam was promoted through impressed current. The accelerated corrosion setup, schematically illustrated in Fig. 2c, was specifically chosen to promote a non-uniform corrosion

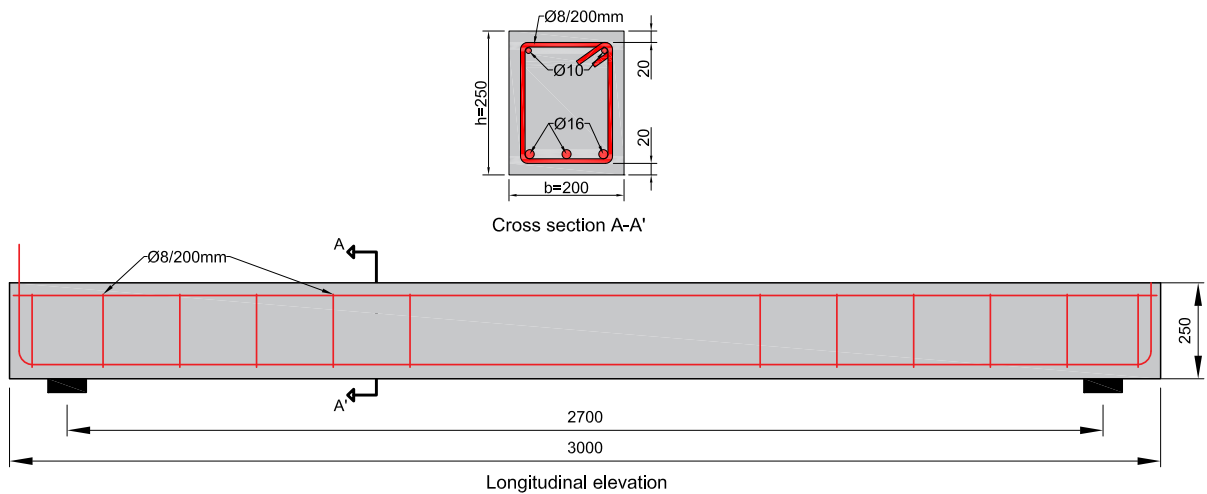


Fig. 1 Geometry of the beam specimen and reinforcement layout (all measurements in mm)

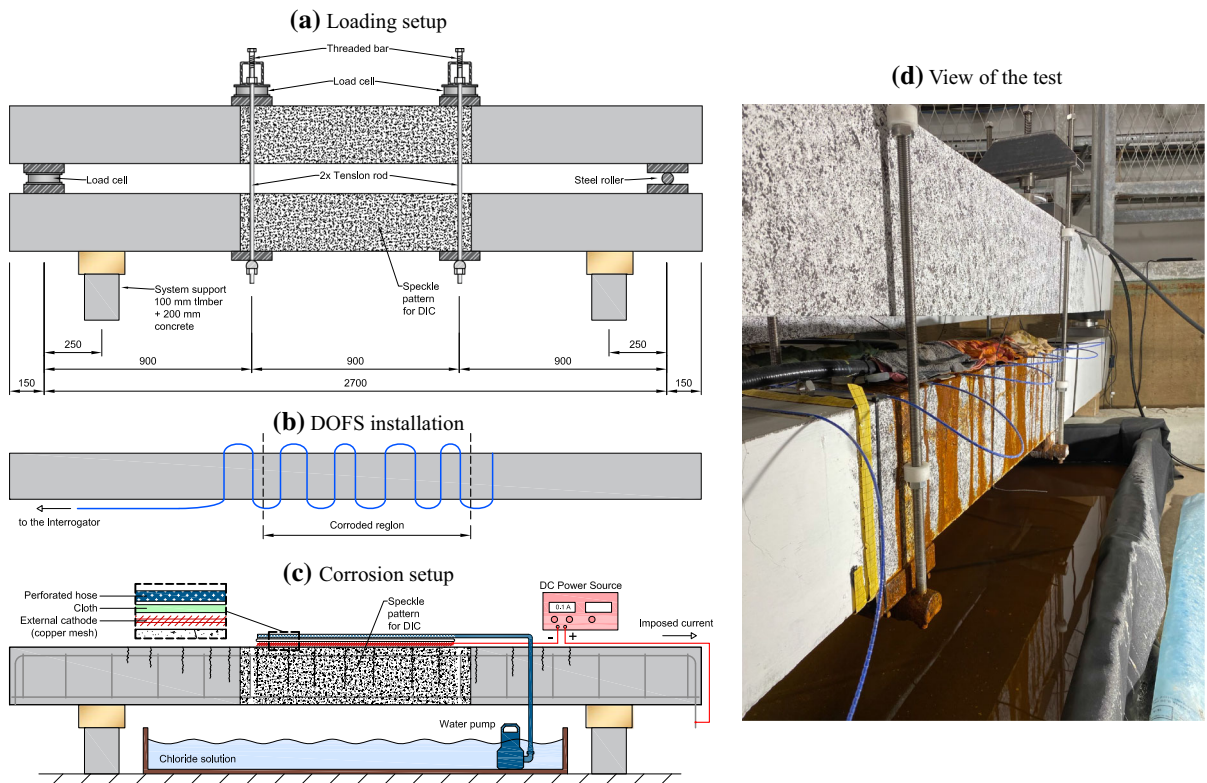


Fig. 2 **a** Loading setup for long-term imposed deformation; **b** schematic representation of the DOFS installation; **c** accelerated corrosion setup with impressed current; **d** view of the test during the accelerated corrosion phase (all measurements are in mm)

distribution. To that end, the three tensile reinforcement bars were electrically connected among them and to the positive terminal of a DC power source. The negative terminal of the source was then connected to

a copper mesh laid along the tensile surface of the beam and reaching between the loading points, which acted as the external cathode. To ensure the electrolytic connection between the external cathode and

the embedded reinforcement, the copper mesh was covered with several pieces of cloth that were intermittently wetted using a perforated hose that pumped chloride solution from a pool placed underneath the beams. The external position of the cathode and the existence of bending cracks was expected to favour the concentration of corrosion in the spots where the reinforcement intersected the cracks, as they will act as the paths of least resistance for the electric current. Chloride solution was pumped for five minutes every 30 min whereas a constant direct current of 0.1 A was applied for 5 weeks, then ceased for 2 weeks and finally applied again for 2 more weeks.

During the accelerated corrosion phase, the initiation and propagation of corrosion-induced cracks on one of the lateral sides of the beam was monitored using DIC. For that purpose, images were taken periodically using a Fujifilm X-T30 digital camera. Each image covered a region of the central part of the beams of approximately 1.2 × 0.8 m and had a size of 26 megapixels, i.e. 6240 × 4160 pixels, delivering a resolution of 0.19 mm/pixel. Images were taken every 2 h during the entire duration of the tests and were later processed and analysed in the commercial software GOM correlate.

Cracks on the tensile face of the beam were monitored using a distributed optical fiber sensor. In this study, a robust fiber optic cable BRUsens V9 from Solifos with an inner steel tube and an external rugged polyamide cladding was used. The cable, with a diameter of 3.2 mm, was deployed as schematically shown in Fig. 2b by gluing the sensor to the surface of the concrete using epoxy resin. The Optical Distributed Sensor Interrogator (ODiSI) 6000 series from Luna Inc. was used as data acquisition unit. The largest available spatial resolution between measuring points provided by the interrogator was chosen, namely 2.6 mm, whereas the sample rate was set at 1 measurement every 10 min. A general view of the test setup is shown in Fig. 2d.

2.3 Characterization of rebar corrosion by 3D laser scanning

2.3.1 Generation of 3D point clouds

Once the accelerated corrosion test was concluded, the corroded beam was removed from the testing rig and

the concrete cover was detached in order to reveal the tensile reinforcement bars. Subsequently, one-meter segments from the centre of the rebar were cut out using a water-cooled circular saw, which were then subjected to a sand-blasting process to remove the remaining adhered corrosion products according to [22].

The clean reinforcement bar segments were then 3D scanned in order to determine the local corrosion level along the rebar length. The scanning of the bars was carried out using a portable laser scanner Handy Scan 700TM from Creaform, featuring an accuracy of up to 30 μm and a maximum spatial resolution of the generated point cloud of 0.05 mm. The result of the 3D scanning consisted of a 3D point cloud that was used to create a triangular mesh describing the surface of the examined bars, as shown in Fig. 3a, b for a corroded and uncorroded bar section, respectively. After processing and repairing the initially obtained mesh to fill small holes and remove possible noise, a new point-cloud was generated to be further analysed using the commercial software Matlab.

Following the methodology presented in [18], a surface interpolation of the point-cloud was carried out after a change of the coordinate system from cartesian to polar, so that rectangular corrosion penetration maps as the ones depicted in Fig. 3c, d, could be generated. This representation of the data facilitates the identification of the areas more heavily affected by corrosion both along the length and around the perimeter of the bar. Next, a description of the longitudinal variation of cross-sectional area along the bar length was performed as the integration of the area enclosed by the surface points. This representation of the data allowed to clearly identify the position of the critical sections, namely the sections featuring the largest sectional loss, as well as to determine their remaining cross-sectional area, see blue line in Fig. 3e.

A further step was implemented to determine the local corrosion level, defined as the loss of cross-sectional area relative to the initial cross-sectional area, according to Eq. (1):

$$\mu = \frac{A_0 - A_{\text{corr}}}{A_0} \times 100 \quad (1)$$

where μ is the local corrosion level, in %, and A_0 and A_{corr} are the uncorroded and corroded bar cross-sectional areas, respectively. To that end, following

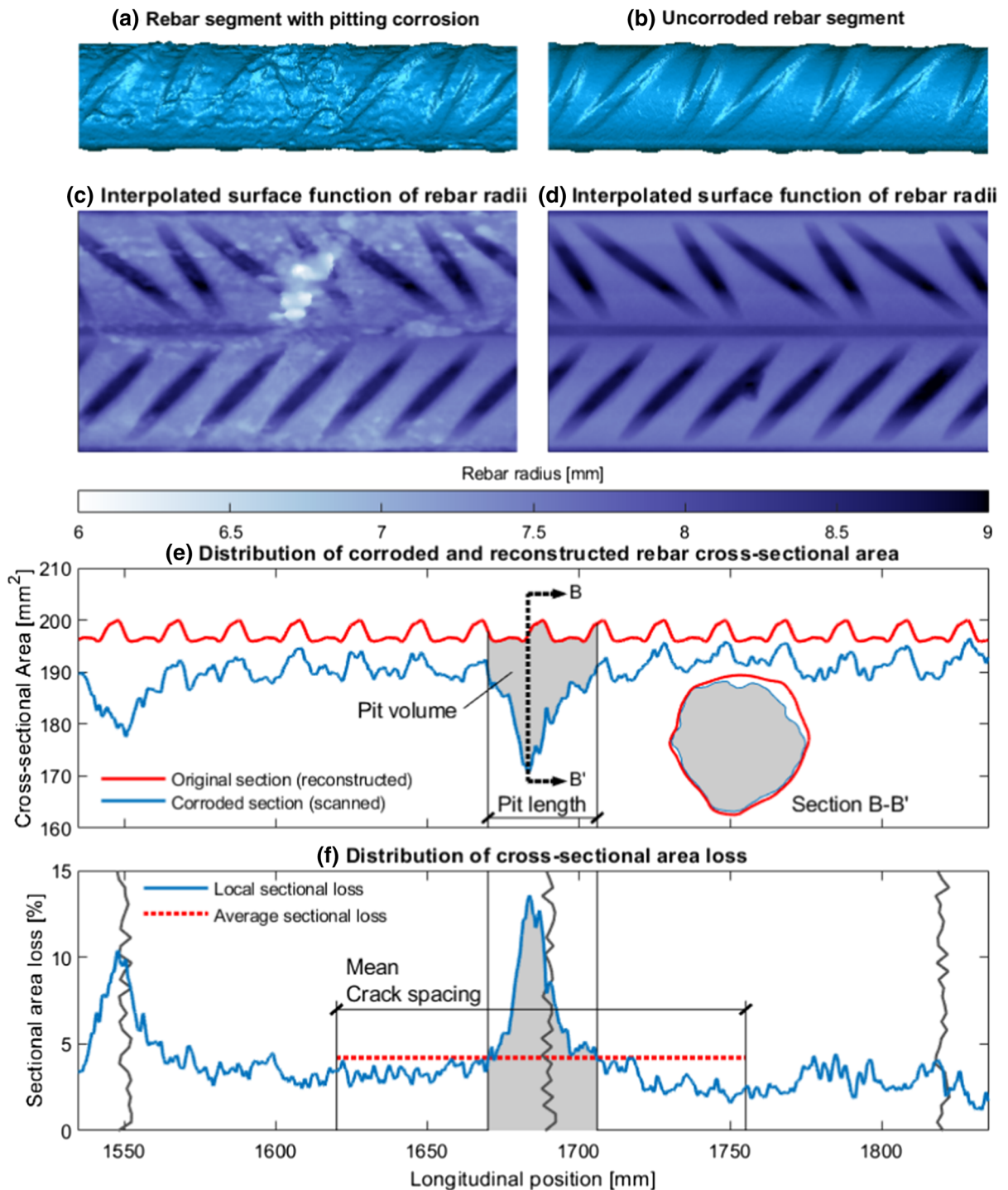


Fig. 3 The resulting triangle mesh from the 3D scanning of **a** a corroded bar section and **b** an uncorroded bar section. Corrosion maps resulting from the interpolated surface function in polar coordinates where the colour indicates the radius for **c** a corroded bar section and **d** an uncorroded bar section. **e** The computed distribution of residual cross-sectional area based on

the interpolated surface from the 3D scanner (blue) and the reconstructed original distribution of cross-sectional areas (red). Section B-B' illustrates the most corroded section for the selected pit. **f** Distribution of focal corrosion level in terms of sectional loss and definition of average corrosion level based on mean crack width and pit length. (Color figure online)

the same principle presented in [20], a reconstruction of the original distribution of cross-sectional area was performed. The reconstruction entailed the concatenation of the average area distribution of a segment taken from healthy parts of the rebar. In particular, the segment comprised the distance between two consecutive points of minimum local cross-section. The result of the reconstructed cross-sectional area is depicted in Fig. 3e as a red line.

2.3.2 Definition of corrosion features

The presented accelerated corrosion setup aimed at achieving a non-uniform corrosion distribution including both regions of localized pitting and regions with more general corrosion. The regions with localized pitting are of special interest since they govern the rate of structural degradation at early stages. Accordingly, it is useful to define certain metrics that allow for a direct comparison between different pits.

The first and most straightforward parameter to define a pit is the maximum local corrosion level, as defined in Eq. (1), at the section with minimum residual cross-sectional area. Even though the maximum corrosion level can be used to obtain a good estimation of the residual capacity of a corroded rebar, that alone might not necessarily be a good indicator of corrosion-induced cracking. In order to take the 3D shape of the pits into account, the corrosion pit volumes were calculated. However, the boundaries of a pit are not well-defined in bars where both localized and pitting corrosion coexist.

In order to establish an objective measure of the pit volume, in this work the pit length was defined as the distance where the local corrosion level exceeded the average corrosion level calculated over the mean crack spacing. This definition is illustrated in Fig. 3f for clarity. Once the pit length is defined, the pit volume is calculated as the integral of the sectional loss over the pit length. Note that this approach assumes that there is only one well-defined pit in the vicinity of each crack, which may hinder its application to more advanced corrosion stages or in cases where corrosion takes place in uncracked concrete.

2.4 Crack width measurements

As previously mentioned, two different techniques were used to measure the crack width of longitudinally

formed cracks on different surfaces of the beam, namely distributed optic fiber sensors and digital image correlation. In the following sections the specifics of each technique and the procedure followed to obtain the crack width are explained.

2.4.1 Measurements based on DOFS

DOFS provide a continuous description of the strain along the fiber sensor. It has been previously shown by the authors [24–26] as well as others [27–29], that the integration of longitudinal strains along a certain length in a beam can be used to accurately determine the crack width of individual bending cracks. The same concept is applied here with the difference that in the present study, the fiber sensors are placed transversally at different sections of the beam. In the case of multiple bending cracks, the integration domain for each crack is commonly assumed to be the mean crack distance centred in the crack. However, since only one crack was detected on the top surface of the beam, in this study the strains were integrated along the entire width of the element.

2.4.2 Measurements based on DIC

DIC enables the tracking of 2D strain fields on the surface of an object over time, which makes it a particularly helpful technique to monitor the formation and growth of cracks in concrete since the large area covered by the images does not require knowing beforehand the position of the cracks. Even though today, the use of DIC is widely spread for common structural tests, monitoring the formation of corrosion-induced cracks poses several challenges. Firstly, the setup needs to be suitable for the use of this technique, i.e., the surface to be monitored needs to be exposed and accessible at all times. Moreover, the appearance of stains stemming from the flow of water mixed with corrosion products on the monitored surface reduces the usable surface area where results can be obtained, see Fig. 4a. Nevertheless, in this work it was possible to define a series of virtual gauges on the surface where accurate results could be obtained over time until the end of the tests. Figure 4b shows the position of the virtual gauges together with the longitudinal crack pattern reconstructed based on linear interpolation between discrete measurements.

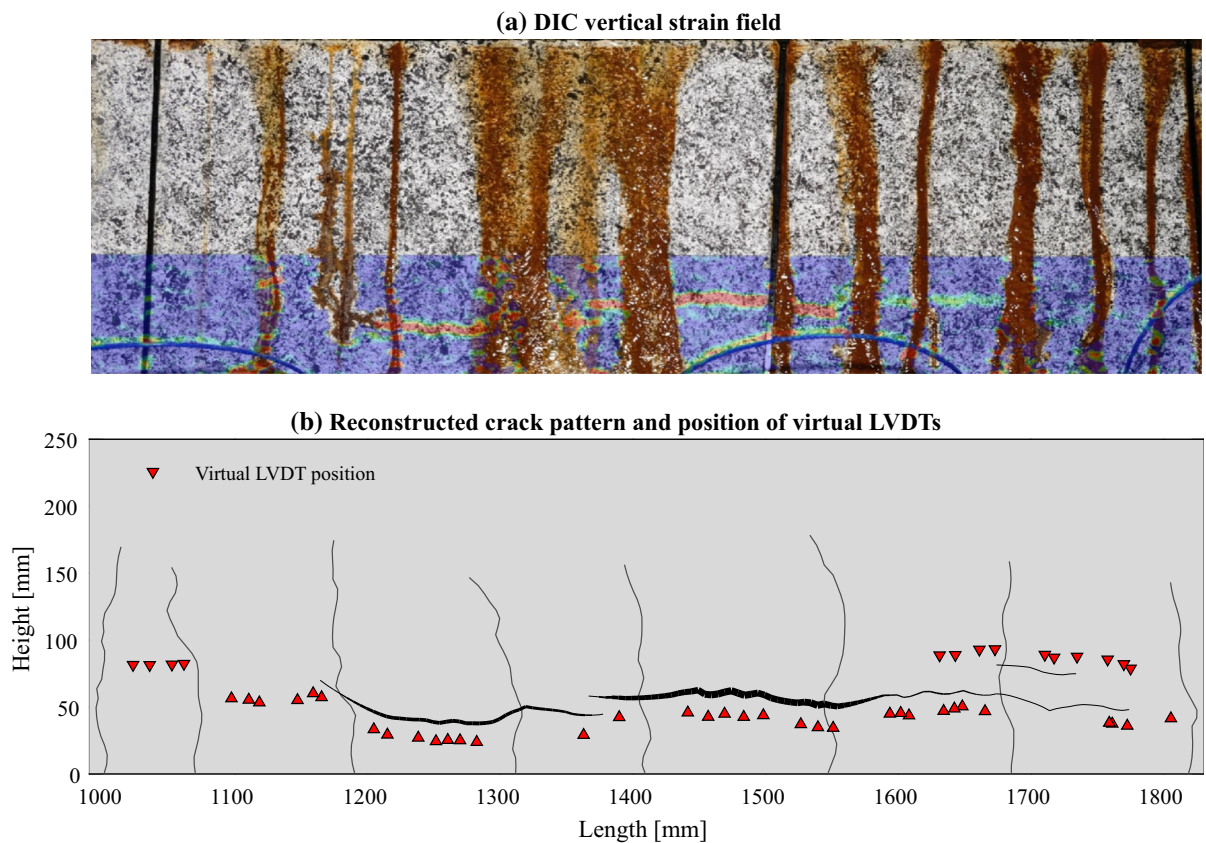


Fig. 4 **a** Example of one of the images used to determine the evolution of corrosion-induced longitudinal cracks with an overlay of DIC postprocessed results showing the field of major principal strains (note that the image is upside down with respect to the testing setup to facilitate the intuitive expectation of the

tensile reinforcement at the bottom of the beam). **b** Reconstruction of the corrosion-induced cracks obtained through interpolation of the discrete measurements carried out at the location of the virtual gauges depicted as red markers

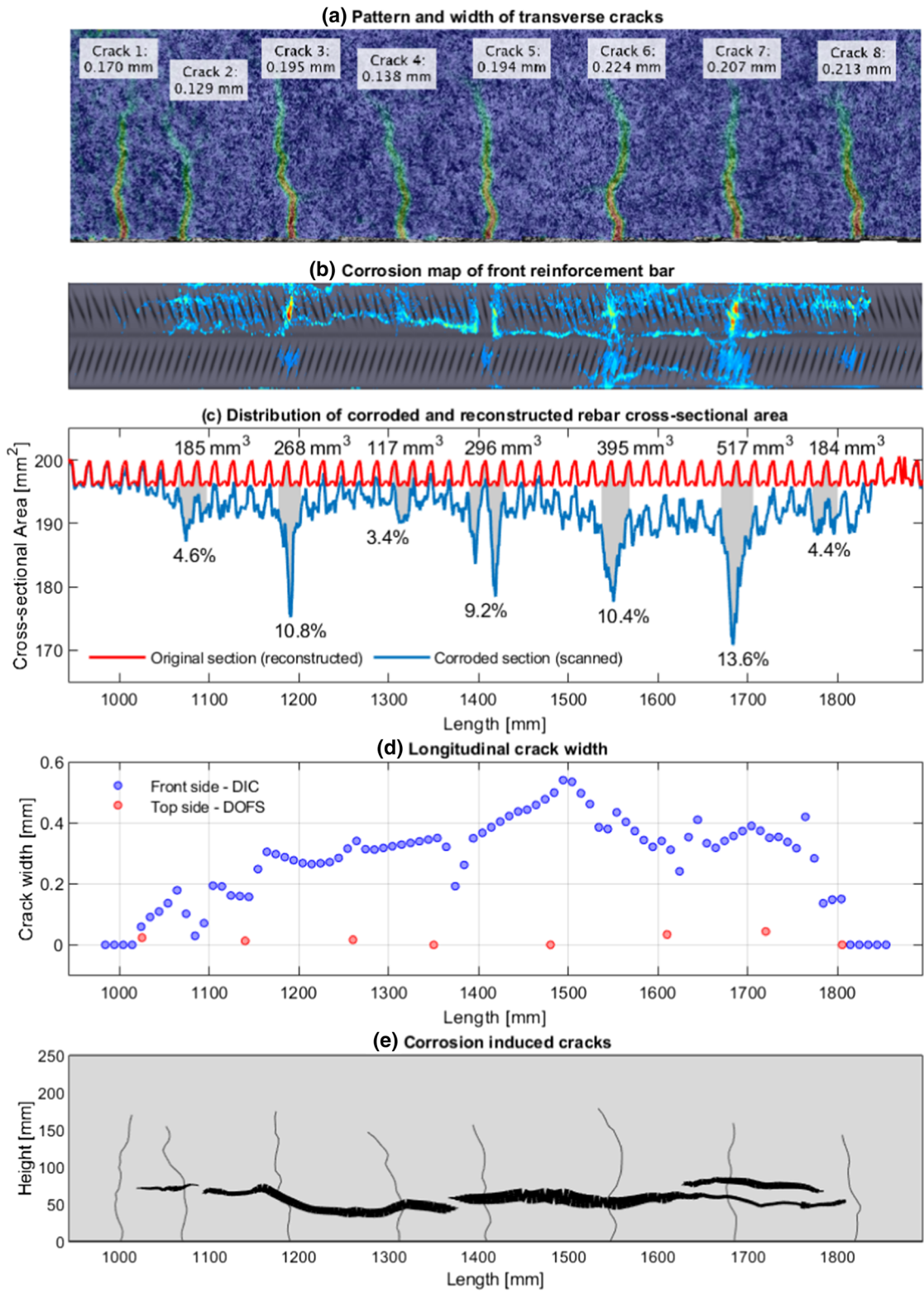
3 Results and discussion

3.1 Linking corrosion of reinforcement to transversal and longitudinal cracking

In Fig. 5, an overview of the experimental results is presented. Figure 5a shows the principal strain field during the loading procedure where the position of the bending cracks in the central part of the beam is highlighted. A total of eight bending cracks were identified which are numbered from 1 to 8 in Fig. 5a. Information about the maximum crack width reached at the crack mouth (bottom surface) is provided. Figure 5b illustrates the distribution of corrosion over the surface of the reinforcement bar that was closest to the side of the DIC measurements (front bar). The parts of the bar in colour represent the areas with

Fig. 5 Overview of results: **a** position and maximum crack width of bending cracks as measured by DIC; **b** corrosion distribution along the surface of the front reinforcement bar based on 3D scanner; **c** variation of original and residual cross-sectional area along the bar and indication of the maximum corrosion level and pit volume of each pit; **d** longitudinal crack width as measured by DOFS and DIC; **e** longitudinal crack pattern at the end of the accelerated corrosion test

apparent corrosion, defined as those points on the surface where the corrosion penetration exceeded 0.2 mm with respect to the reconstructed original surface. Figure 5c presents the variation of the original and residual cross-sectional area for the bar displayed in Fig. 5b, where the maximum corrosion level and the volume of each pit have been specified. Figure 5d shows the variation of the accumulated longitudinal



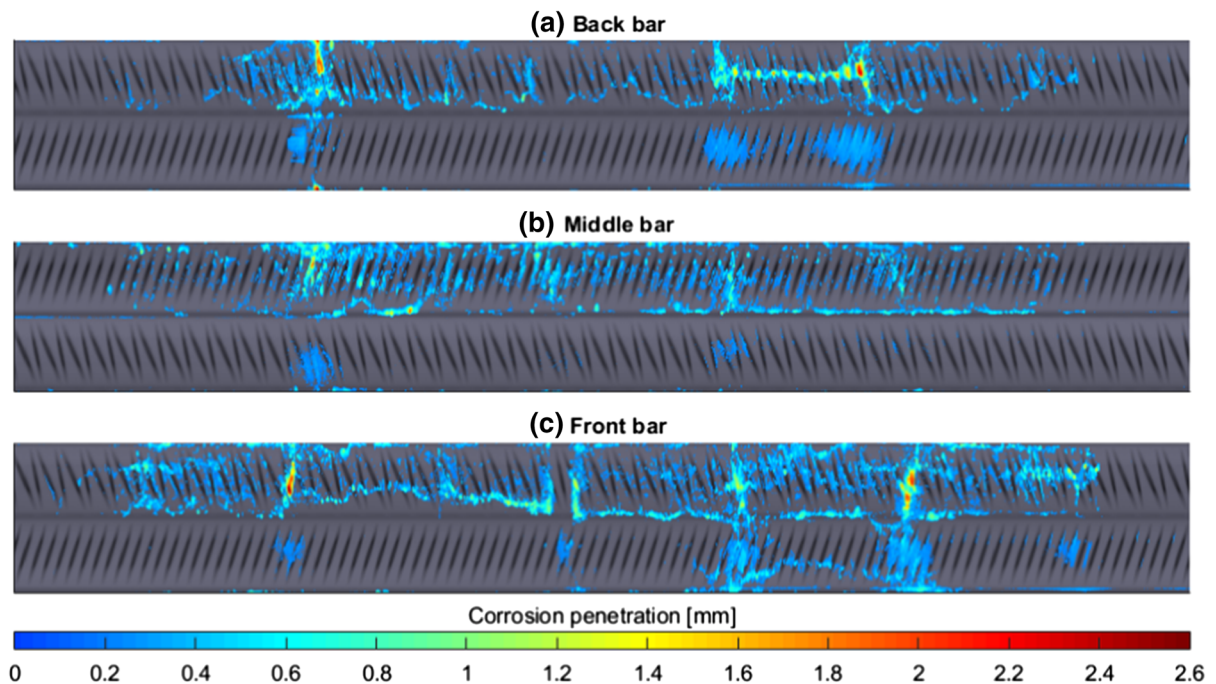


Fig. 6 Corrosion maps displaying the distribution of corrosion penetration for **a** the back reinforcement bar, **b** the middle reinforcement bar and **c** the front reinforcement bar

crack width as measured by the DOFS and DIC on the top and lateral sides of the beam, respectively. Finally, Fig. 5e displays a reconstruction of the crack pattern at the end of the test based on DIC measurements for the longitudinal cracks formed on the lateral side of the beam.

Several findings can be observed in Fig. 5. First, the proposed experimental setup for accelerated corrosion could successfully deliver a non-uniform distribution of corrosion along the reinforcement bars. Not only that, but the presence of corrosion pits in the bar was clearly governed by the existence of bending cracks as suggested by the close agreement between their respective positions along the bar. This correlation between the position of cracks and pits in reinforcement bars is in line with previous findings observed in naturally corroded elements for early stages of corrosion [20, 30]. This suggests that the setup put forth can be used to reproduce realistic corrosion distributions, up to moderate corrosion levels, which can be of interests in laboratory studies aimed at investigating the load bearing capacity of corroded structures. It should be noted, however, that when using impressed current the composition of the generated corrosion products may still differ from those generated under

natural conditions, thereby changing their volumetric ratio and therefore modifying the rate of corrosion-induced degradation. To further support the validity of the observed results, the corrosion distribution on the three reinforcement bars is presented in Fig. 6, where it can be seen that corrosion concentrated at the location of transverse cracks in all bars.

Regarding the relationship between longitudinal cracking and corrosion, a clear relation becomes also apparent between the extent of longitudinal crack propagation and the length of reinforcement bar with appreciable corrosion, being the regions beyond those areas free of corrosion-induced cracking. It is interesting to note that the longitudinal cracks formed on the lateral side were somewhat higher than the tensile reinforcement, the centre of which was at about 36 mm from the bottom. This could be caused by the presence of an earlier longitudinal crack formed at the tensile surface of the beam, which might have conditioned the position of subsequent cracks.

The relationship between the crack width of transversal cracks and the extent of corrosion at the pits in terms of maximum corrosion level and pit volume is explicitly presented in Fig. 7a, b, respectively, where each marker has been numbered

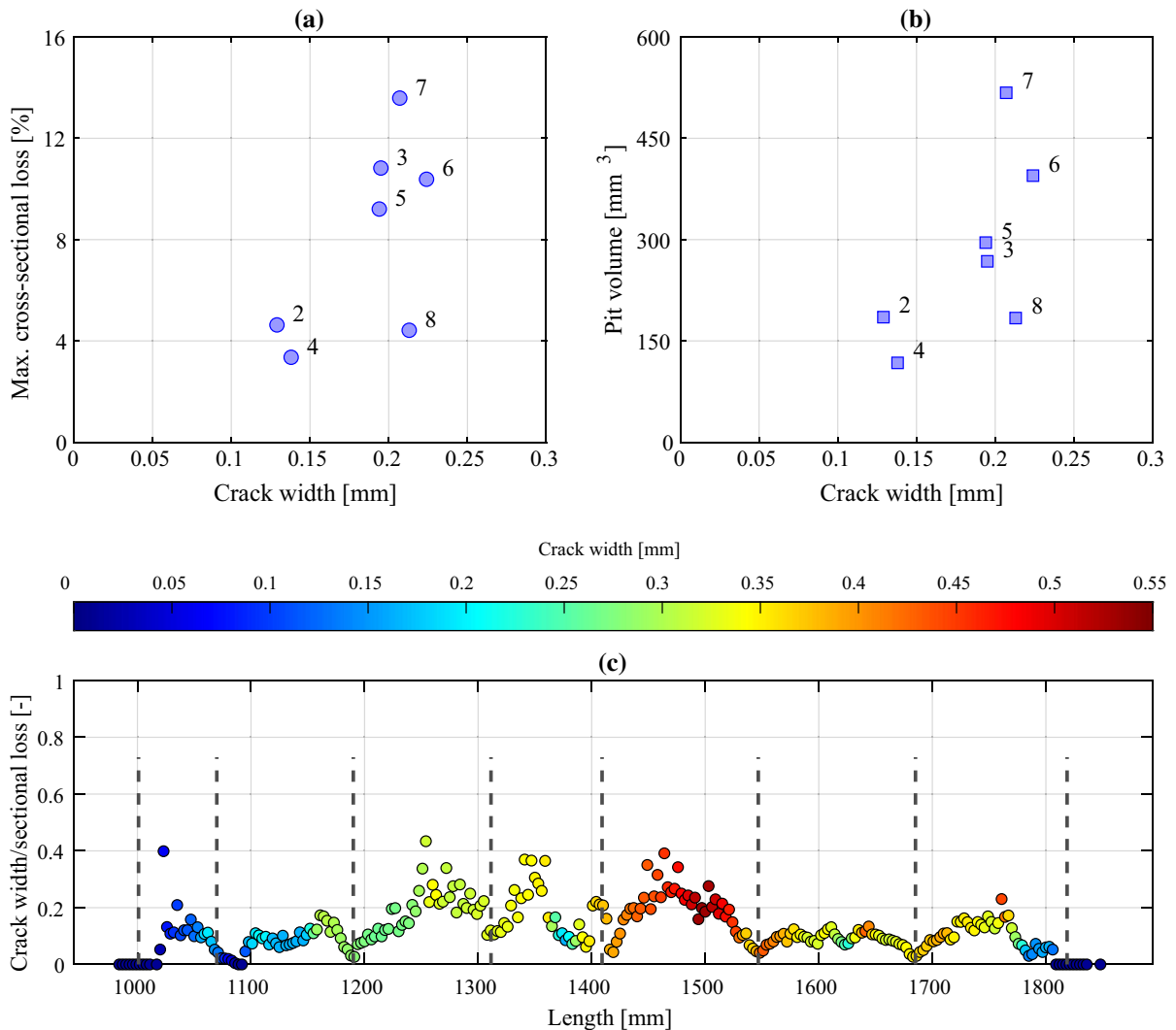


Fig. 7 **a** Relationship between transversal crack width and maximum corrosion level at the pit; **b** relationship between transversal crack width and pit volume; **c** ratio between

longitudinal crack width and corrosion level along the length of the reinforcement bar. Dashed lines indicate the position of transversal cracks and pits

according to the crack number shown in Fig. 5a. Note that crack 1 is not included because no corrosion was found at that location. This is most likely due to the fact that the external cathode did not reach the position of crack 1. For the rest of cracks, it can be observed that both the maximum corrosion level and the pit volume were quite sensitive to the transversal crack width. Indeed, varying the crack width from 0.13 to 0.22 mm had a remarkable effect on the amount of steel loss at the pit, which increased by almost a factor of three. This indicates that crack width played a major

role in how externally impressed current was distributed by ionic migration through transversal cracks.

However, the condition at the steel–concrete interface, which is known to have a decisive role in the corrosion of reinforcement [31] and which is directly related to the surface crack width by the bond-slip behaviour of the rebar could be the main factor driving the distribution of corrosion at the pits. It should also be highlighted that crack 8, which is at the other end of the investigated region, might have suffered from a similar issue as described for crack 1, which could have hindered the development of corrosion at that

location, hence a slightly discrepant tendency with respect to the rest of data points.

In order to investigate whether a relationship exists between the longitudinal crack width and the distribution of corrosion along the reinforcement, the ratio between the crack width and maximum corrosion level at each section of the bar is presented in Fig. 7c. As observed, the highly variable profile of the plotted ratio suggests that a local relationship does not exist. Indeed, comparing Fig. 5c, d, it can be seen that whereas the longitudinal crack width exhibits a certain continuity along its length, the corrosion level is highly irregular with large spatial gradients. As a result, the crack width-corrosion level ratio becomes very small at the location of the pits where the corrosion level is significantly higher. On the other hand, away from the cracks, the ratio becomes larger due to the significantly lower corrosion levels. These results reveal that unlike in elements with generalized corrosion where the steel loss occurs uniformly along the surface of the bars, the width of longitudinal cracks cannot be directly correlated with the local corrosion level of the reinforcement in cases where non-uniform corrosion prevails. Furthermore, this implies that in elements with transverse cracks where an ongoing corrosion exists, it is not possible to determine the most corroded section solely based on the examination of the crack width of longitudinal cracks, which is in line with the findings by [8]. Conversely, the crack width of corrosion-induced cracks seems to be a function of the accumulated or total corrosion along the corroded region.

3.2 Evolution of corrosion-induced cracks

3.2.1 Crack width

In the previous section it was shown that the longitudinal crack width could not be related to the local corrosion level at a given point in time and, instead, the global amount of corrosion in a wider region must be considered. In this section, the variation of crack width over time is investigated. The evolution of the width of corrosion-induced cracks is presented in Fig. 8a, c at eight individual points of the bottom and lateral sides of the beam, respectively, which are indicated in Fig. 8b. Additionally, in Fig. 8c, vertical dashed lines have been included to indicate different times of interest, where the times from t_1 to t_6

correspond to the appearance of new longitudinal cracks (i.e., not having a continuous path with existing ones) whereas t_7 and t_8 represent the start of the second impressed current period and the end of the test, respectively.

As observed in Fig. 8a, cracking at the bottom surface of the beam occurred approximately 10 days after the initiation of the accelerated corrosion process. It should be noted that the calculated crack width displayed in Fig. 8a up to that point corresponds to the elastic expansion of the concrete before cracking. Subsequently, cracks at the bottom surface grow proportionally with increasing time, although at different rates, up to a period of about 20 days, after which they either stabilize or reclose. This change in the growth rate coincides with the appearance of longitudinal cracks on the lateral side of the beam, as shown in Fig. 8c. Due to the layout of the reinforcement and the corrosion of three tensile reinforcement bars forming a horizontal plane, most of the corrosion-induced damage was concentrated on the longitudinal cracks formed on the lateral side beam, rendering the cracks at the bottom surface almost negligible.

Looking at the evolution of the crack width for the longitudinal cracks on the lateral side, it can be seen that in all cases the crack width increases almost linearly with time while it halts during the period where impressed current ceases. Moreover, after restarting the impressed current, the crack width of longitudinal cracks started to increase again with a similar linear trend. Since the externally applied current was kept constant during the periods of impressed current, and assuming that the distribution of corrosion rates along the bar did not change significantly after the formation of the longitudinal cracks, it can be inferred from the results in Fig. 8c that changes in corrosion-induced crack width are proportional to changes in local corrosion levels. However, the factor of proportionality between crack width and the local corrosion level does not remain constant at different sections and it is most likely influenced by both the local mechanical properties of the concrete as well as the distribution of corrosion in the neighbouring zone of the investigated section. Nevertheless, these results suggest that if the corrosion level could be assessed at two different points in time, then the factor of proportionality between the longitudinal crack width and the corrosion rate could be established. Once the factor of proportionality is



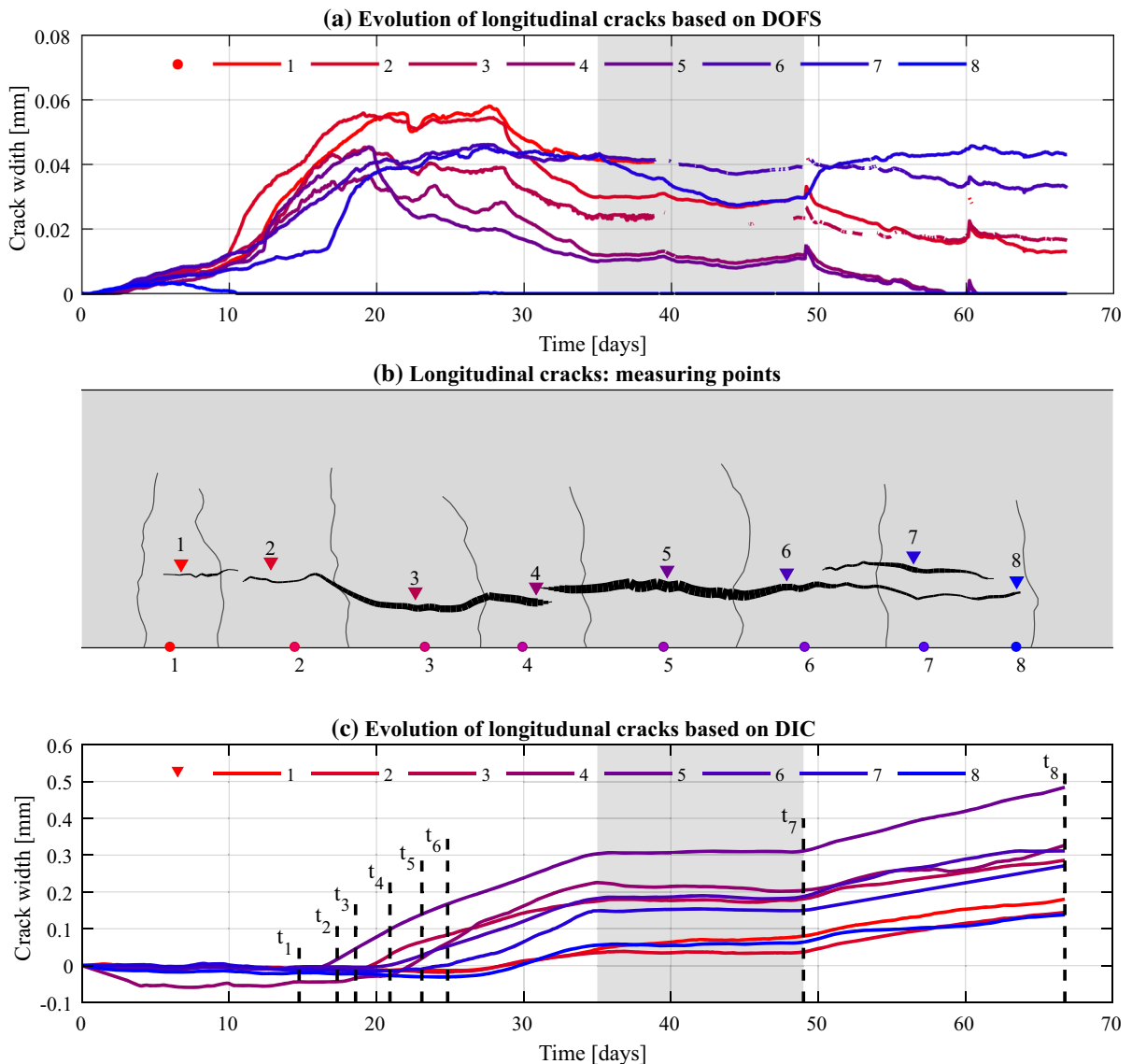


Fig. 8 **a** Crack width evolution of longitudinal cracks formed on the tensile surface of the beam based on DOFS measurements; **b** longitudinal crack pattern on the lateral side of the beam. The markers indicate the position at which cracks have

been measured for the DOFS (●) and DIC (▲); **c** crack width evolution of longitudinal cracks formed on the lateral side of the beam based on DIC measurements

known, the monitoring of longitudinal cracks could be used to determine the rate of reinforcement corrosion at any time.

3.2.2 Crack pattern

It could already be observed from Fig. 8 that longitudinal cracks on the lateral side of the beam initiated earlier in the central region of the investigated area

compared to those present near the edges. Moreover, together with the distribution of the crack width, that clearly indicates that longitudinal cracks initiated in the centre and propagated towards the sides. However, owing to the availability of DIC measurements, it was possible to analyse in detail the evolution of the longitudinal crack pattern, which is presented in Fig. 9 for the eight different times highlighted in Fig. 8c,

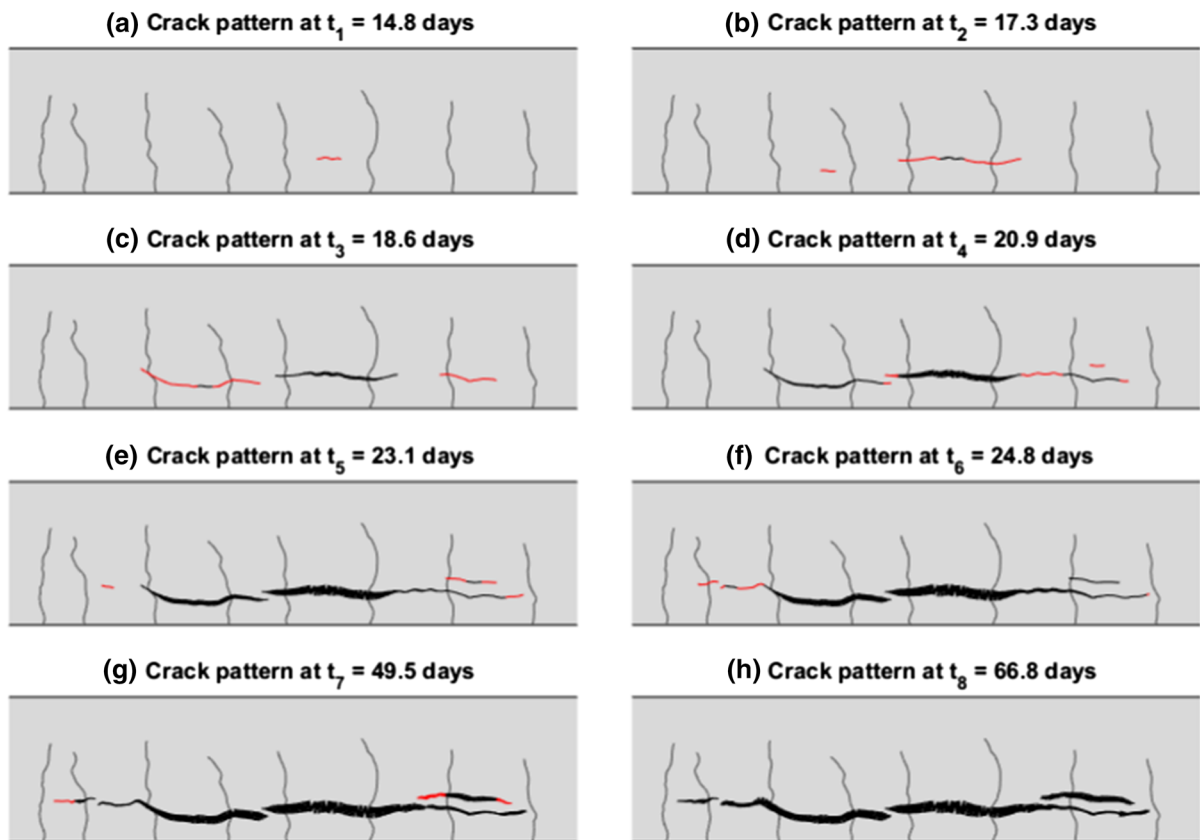


Fig. 9 Evolution of the corrosion-induced longitudinal crack pattern as measured per DIC. Red crack segments indicate new cracks with respect to the previous time step. (Color figure online)

where the crack segments drawn in red represent cracks that were not present in the previous step.

The results in Fig. 9 confirm that longitudinal cracking initiated at the centre of the investigated region. However, it can also be observed that longitudinal cracks initiated at different locations over time and subsequently merged. This could be different from a natural corrosion scenario where corrosion focuses in a smaller region as opposed to the present study where corrosion happened along the entire investigated area.

Another finding from Fig. 9 is the fact that, contrary to what could be anticipated, longitudinal cracks did not initiate at the sections with a greater local corrosion level. Instead, new cracks were in most cases observed to form in the regions between transversal cracks, which as previously discussed, featured relatively low corrosion levels. An explanation for this observation could be found in the transport of corrosion products through transversal cracks,

which were open due to the applied load, thereby relieving most of the stress stemming from the accumulation of rust in the cracked sections. Conversely, in regions without transversal cracks, despite displaying a visibly lower corrosion level, the absence of cracks led to the confinement of corrosion products and the raise of stresses, thus causing an earlier initiation of cracks. This observation clearly shows that the mechanical action exerted by the corrosion products plays a more important role on corrosion induced cracking than the extent of corrosion itself. It should be noted, however, that the observed behaviour was influenced by the particular conditions of the test setup and the experimental procedure. On the one hand, inducing corrosion through impressed current might have played a role, since a faster rate of iron dissolution can result in the formation of more soluble corrosion products due to lack of oxygen availability at the steel concrete interface. Moreover, in the experiments, cracks were held open which facilitated

the flow of corrosion products through them. Natural corrosion, on the other hand, takes place at a significantly lower rate while cracks in real structures may not be open at all times, thereby increasing the probability of cracks being sealed by corrosion products.

4 Conclusions

In this article a thorough investigation was carried out to elucidate the interplay between corrosion of reinforcement and cracking in reinforced concrete structures with non-uniform corrosion distribution. To that end, experimental tests were carried out and advanced measurement techniques were used to monitor the formation and propagation of concrete cracks as well as to characterize the corrosion of reinforcement. The following conclusions can be drawn:

1. The proposed experimental setup was able to successfully reproduce realistic corrosion distributions exhibiting corrosion pits at the location of transverse cracks, which could be used to study the load bearing capacity of corroded concrete structures in the laboratory. Moreover, it has been found that the crack width of transversal cracks has a strong impact on the local corrosion level and pit volume when impressed current is used to induce corrosion with an external cathode.
2. Unlike for elements exhibiting uniform corrosion, a direct correlation cannot be established between the width of longitudinal cracks and the local corrosion level of elements with non-uniform corrosion. Consequently, in reinforced concrete elements where reinforcement is actively corroding, it is in general not feasible to discern the most corroded section solely based on the examination of corrosion-induced cracks.
3. After the formation of corrosion-induced cracks, it was found that their width increased linearly with the local corrosion level provided the distribution of corrosion did not change significantly. This entails that the opening of longitudinal cracks can be used to monitor the rate of corrosion degradation given their propagation has stabilized.
4. Despite corrosion was found to concentrate at the location of transversal cracks, the transport of corrosion products through the open cracks and subsequent relief of internal stress caused the longitudinal cracks to form predominantly in the regions between transversal cracks. This indicates that the extent of corrosion correlates to longitudinal cracking through the mechanical effect of corrosion products, which highlights that detecting the location of corrosion-induced crack initiation might not be indicative of the position of the most corroded section.

Funding Open access funding provided by Chalmers University of Technology. This research has been performed as part of the project: ‘Sensor-driven cloud-based strategies for infrastructure Management—SensIT’ funded by the Swedish Transport Administration (Trafikverket) under the grant TRV/BBT 2017-028.

Declarations

Conflict of interest The authors declare that they have no conflict of interest.

Open Access This article is licensed under a Creative Commons Attribution 4.0 International License, which permits use, sharing, adaptation, distribution and reproduction in any medium or format, as long as you give appropriate credit to the original author(s) and the source, provide a link to the Creative Commons licence, and indicate if changes were made. The images or other third party material in this article are included in the article’s Creative Commons licence, unless indicated otherwise in a credit line to the material. If material is not included in the article’s Creative Commons licence and your intended use is not permitted by statutory regulation or exceeds the permitted use, you will need to obtain permission directly from the copyright holder. To view a copy of this licence, visit <http://creativecommons.org/licenses/by/4.0/>.

References

1. Bertolini L, Elsener B, Pedferri P, Polder R (2004) Corrosion of steel in concrete, repair. Wiley-VCH Verlag, Germany
2. Beeby AW (1983) Cracking, cover and corrosion of reinforcement. *Concr Int* 5:35–40
3. Berrocal CG, Löfgren I, Lundgren K, Tang L (2015) Corrosion initiation in cracked fibre reinforced concrete: influence of crack width, fibre type and loading conditions. *Corros Sci* 98:128–139. <https://doi.org/10.1016/j.corsci.2015.05.021>
4. Fernandez I, Herrador MF, Marí AR, Bairán JM (2018) Ultimate capacity of corroded statically indeterminate reinforced concrete members. *Int J Concr Struct Mater*. <https://doi.org/10.1186/s40069-018-0297-9>
5. Gowers KR, Millard SG (1999) Electrochemical techniques for corrosion assessment of reinforced concrete structures.



- Proc Inst Civ Eng Struct Build 134:129–137. <https://doi.org/10.1680/istbu.1999.31379>
6. Coronelli D, Hanjari KZ, Lundgren K, Rossi E (2011) Severely corroded reinforced concrete with cover cracking: part 1. Crack Initiation Propag RILEM Bookseries 5:195–205. https://doi.org/10.1007/978-94-007-0677-4_13
 7. Al-Harthy AS, Stewart MG, Mullard J (2011) Concrete cover cracking caused by steel reinforcement corrosion. *Mag Concr Res* 63:655–667. <https://doi.org/10.1680/macrc.2011.63.9.655>
 8. Yu L, François R, Dang VH, L’Hostis V, Gagné R (2015) Distribution of corrosion and pitting factor of steel in corroded RC beams. *Constr Build Mater* 95:384–392. <https://doi.org/10.1016/j.conbuildmat.2015.07.119>
 9. Andrade C, Alonso C, Molina FJ (1993) Cover cracking as a function of bar corrosion: part I-experimental test. *Mater Struct* 26:453–464. <https://doi.org/10.1007/BF02472805>
 10. Cairns J, Du Y, Law D (2008) Structural performance of corrosion-damaged concrete beams. *Mag Concr Res* 60:359–370. <https://doi.org/10.1680/macrc.2007.00102>
 11. El Maaddawy T, Soudki K, Topper T (2005) Long-term performance of corrosion-damaged reinforced concrete beams. *ACI Struct J* 102:649–656
 12. Richard B, Quiertant M, Bouteiller V, Adelaide L, Tailhan JL, Cremona C (2012) Influence of accelerated corrosion on the reinforced cover concrete cracking behavior: experimental and numerical study. *Eur J Environ Civ Eng* 16:450–459. <https://doi.org/10.1080/19648189.2012.667997>
 13. Rodriguez J, Ortega LM, Casal J (1997) Load carrying capacity of concrete structures with corroded reinforcement. *Constr Build Mater* 11:239–248. [https://doi.org/10.1016/S0950-0618\(97\)00043-3](https://doi.org/10.1016/S0950-0618(97)00043-3)
 14. Torres-Acosta AA, Martinez-Madrid M (2003) Residual life of corroding reinforced concrete structures in marine environment. *J Mater Civ Eng* 15:344–353. [https://doi.org/10.1061/\(asce\)0899-1561\(2003\)15:4\(344\)](https://doi.org/10.1061/(asce)0899-1561(2003)15:4(344))
 15. Torres-Acosta AA, Sagüés AA (2004) Concrete cracking by localized steel corrosion—geometric effects. *ACI Mater J* 101:501–507
 16. Vidal T, Castel A, François R (2004) Analyzing crack width to predict corrosion in reinforced concrete. *Cem Concr Res* 34:165–174. [https://doi.org/10.1016/S0008-8846\(03\)00246-1](https://doi.org/10.1016/S0008-8846(03)00246-1)
 17. Andrade C, Cesetti A, Mancini G, Tondolo F (2016) Estimating corrosion attack in reinforced concrete by means of crack opening. *Struct Concr* 17:533–540. <https://doi.org/10.1002/suco.201500114>
 18. Tahershamsi M, Fernandez I, Lundgren K, Zandi Hanjari K (2016) Investigating correlations between crack width, corrosion level and anchorage capacity. *Struct Infrastruct Eng* 2479:1–14
 19. Torres-Acosta AA, Navarro-Gutierrez S, Terán-Guillén J (2007) Residual flexure capacity of corroded reinforced concrete beams. *Eng Struct* 29:1145–1152
 20. Berrocal CG, Löfgren I, Lundgren K (2018) The effect of fibres on steel bar corrosion and flexural behaviour of corroded RC beams. *Eng Struct* 163:409–425. <https://doi.org/10.1016/j.engstruct.2018.02.068>
 21. Chen E, Berrocal CG, Fernandez I, Löfgren I, Lundgren K (2020) Assessment of the mechanical behaviour of reinforcement bars with localised pitting corrosion by digital image correlation. *Eng Struct* 219:110936
 22. Fernandez I, Lundgren K, Zandi K (2018) Evaluation of corrosion level of naturally corroded bars using different cleaning methods, computed tomography, and 3D optical scanning. *Mater Struct Constr* 51:1–13. <https://doi.org/10.1617/s11527-018-1206-z>
 23. EN 12390-3:2009 Testing hardened concrete. Part 3: compressive strength of test specimens (2009)
 24. Berrocal CG, Fernandez I, Bado MF, Casas JR, Rempling R (2021) Assessment and visualization of performance indicators of reinforced concrete beams by distributed optical fibre sensing. *Struct Heal Monit.* <https://doi.org/10.1177/1475921720984431>
 25. Berrocal CG, Fernandez I, Rempling R (2021) Crack monitoring in reinforced concrete beams by distributed optical fiber sensors. *Struct Infrastruct Eng* 17:124–139. <https://doi.org/10.1080/15732479.2020.1731558>
 26. Bado MF, Casas JR, Dey A, Berrocal CG (2020) Distributed optical fiber sensing bonding techniques performance for embedment inside reinforced concrete structures. *Sensors (Switzerland)* 20:1–23. <https://doi.org/10.3390/s20205788>
 27. Brault A, Hoult N (2019) Monitoring reinforced concrete serviceability performance using fiber-optic sensors. *ACI Struct J* 116:57–70
 28. Brault A, Hoult N (2019) Distributed reinforcement strains: measurement and application. *ACI Struct J* 1:1. <https://doi.org/10.14359/51714483>
 29. Barrias A, Casas J, Villalba S (2018) Embedded distributed optical fiber sensors in reinforced concrete structures—a case study. *Sensors* 18:980. <https://doi.org/10.3390/s18040980>
 30. Chen E, Berrocal CG, Löfgren I, Lundgren K (2020) Correlation between concrete cracks and corrosion characteristics of steel reinforcement in pre-cracked plain and fibre-reinforced concrete beams. *Mater Struct Constr.* <https://doi.org/10.1617/s11527-020-01466-z>
 31. Angst UM, Geiker MR, Michel A, Gehlen C, Wong H, Isgor OB, Elsener B, Hansson CM, François R, Hornbostel K, Polder R, Alonso MC, Sanchez M, Correia MJ, Criado M, Sagüés A, Buenfeld N (2017) The steel–concrete interface. *Mater Struct* 50:143. <https://doi.org/10.1617/s11527-017-1010-1>

Publisher’s Note Springer Nature remains neutral with regard to jurisdictional claims in published maps and institutional affiliations.

